Nanoscale Advances

ROYAL SOCIETY OF CHEMISTRY

PAPER

View Article Online
View Journal | View Issue

Cite this: *Nanoscale Adv.*, 2023, **5**, 6678

Insight into the electronic structure of the centrosymmetric skyrmion magnet $GdRu_2Si_2$†

S. V. Eremeev, *[a] D. Glazkova,[b] G. Poelchen, [c] A. Kraiker,[d] K. Ali,[e] A. V. Tarasov,[bi] S. Schulz,[c] K. Kliemt, [d] E. V. Chulkov, [bfgh] V. S. Stolyarov,[ijk] A. Ernst, [l] C. Krellner, [d] D. Yu. Usachov [bik] and D. V. Vyalikh *[hm]

The discovery of a square magnetic-skyrmion lattice in $GdRu_2Si_2$, with the smallest so far found skyrmion size and without a geometrically frustrated lattice, has attracted significant attention. In this work, we present a comprehensive study of surface and bulk electronic structures of $GdRu_2Si_2$ by utilizing momentum-resolved photoemission (ARPES) measurements and first-principles calculations. We show how the electronic structure evolves during the antiferromagnetic transition when a peculiar helical order of 4f magnetic moments within the Gd layers sets in. A nice agreement of the ARPES-derived electronic structure with the calculated one has allowed us to characterize the features of the Fermi surface (FS), unveil the nested region along k_z at the corner of the 3D FS, and reveal their orbital compositions. Our findings suggest that the Ruderman–Kittel–Kasuya–Yosida interaction plays a decisive role in stabilizing the spiral-like order of Gd 4f moments responsible for the skyrmion physics in $GdRu_2Si_2$. Our results provide a deeper understanding of electronic and magnetic properties of this material, which is crucial for predicting and developing novel skyrmion-based systems.

Received 20th June 2023
Accepted 16th October 2023

DOI: 10.1039/d3na00435j

rsc.li/nanoscale-advances

1 Introduction

The centrosymmetric antiferromagnet $GdRu_2Si_2$ (T_N of ~46 K), which crystallizes in the $ThCr_2Si_2$ structure with $I4/mmm$ symmetry[1–3] is well known from the early 1980s. Recently, it has returned to the focus of research efforts with the discovery of a square magnetic skyrmion lattice without a geometrically frustrated lattice.[4] This skyrmion phase appears in an external magnetic field of 2–2.5 T at temperatures below 20 K. Although the magnetic properties of $GdRu_2Si_2$ have been studied in great detail over the years,[1–3,5–9] the appearance of the skyrmion phase has renewed and intensified the discussions about this material, especially concerning the reason and origin of skyrmion physics.[4,10–13] It is worth noting that the discovered square skyrmion lattice has a constant of 1.9 nm, the smallest skyrmion size observed to date, which makes it attractive for the development of next-generation high-density, low-power magnetic memory devices.[4,11]

For further studies on the properties of this material and prediction of possible candidates which could reveal unusual magnetic-skyrmion properties as well, detailed information about surface and bulk electronic structures and, most importantly, on how the electronic structure gets modified upon the antiferromagnetic transition is highly desirable. The latter can be derived from momentum-resolved photoemission (ARPES) measurements combined with *ab initio* calculations. The curious question here is in how far it is possible to detect the stabilization of the helical long-range in-plane magnetic order of Gd 4f moments appearing at the zero magnetic field in the ARPES patterns. The next essential question is about the Fermi surface (FS) and its intrinsic properties. Recently, contradicting results were presented for the properties of the three-dimensional (3D) FS. In a recent theoretical study,[10] the

[a]*Institute of Strength Physics and Materials Science, Russian Academy of Sciences, 634055 Tomsk, Russia. E-mail: eremeev@ispms.tsc.ru*
[b]*St. Petersburg State University, 7/9 Universitetskaya Nab., St. Petersburg, 199034, Russia*
[c]*Institut für Festkörper- und Materialphysik, Technische Universität Dresden, D-01062 Dresden, Germany*
[d]*Kristall- und Materiallabor, Physikalisches Institut, Goethe-Universität Frankfurt, Max-von-Laue Strasse 1, D-60438 Frankfurt am Main, Germany*
[e]*Department of Microtechnology and Nanoscience, Chalmers University of Technology, Göteborg, 41296, Sweden*
[f]*Departamento de Polímeros y Materiales Avanzados: Física, Química y Tecnología, Facultad de Ciencias Químicas, Universidad del País Vasco UPV/EHU, 20080 San Sebastián/Donostia, Spain*
[g]*Centro de Física de Materiales (CFM-MPC), Centro Mixto CSIC-UPV/EHU, 20018 San Sebastián/Donostia, Spain*
[h]*Donostia International Physics Center (DIPC), 20018 Donostia-San Sebastián, Spain. E-mail: denis.vyalikh@dipc.org*
[i]*Moscow Institute of Physics and Technology, Institute Lane 9, Dolgoprudny, Russia*
[j]*Dukhov Research Institute of Automatics (VNIIA), Moscow, 127055, Russia*
[k]*National University of Science and Technology MISIS, Moscow, 119049, Russia*
[l]*Institute for Theoretical Physics, Johannes Kepler University, Linz, Austria*
[m]*IKERBASQUE, Basque Foundation for Science, 48011 Bilbao, Spain*

† Electronic supplementary information (ESI) available: Details on bulk electronic structure calculations and magnetic interaction. See DOI: https://doi.org/10.1039/d3na00435j

nested region near the Γ-point was manifested and it was declared to be responsible for the skyrmion physics in $GdRu_2Si_2$. However, the results of ref. 14, which also present a detailed overview of the actual discussion about the properties of $GdRu_2Si_2$, do not confirm the nested region near the Γ-point. This calls for a direct experimental visualization of the Fermi surface and further exploration of its properties *via* ARPES measurements.

Here, we present a detailed study of the electronic structure and discuss FS properties for $GdRu_2Si_2$ obtained from ARPES measurements and *ab initio* density functional theory (DFT) calculations. The latter has been performed for the bulk and for a finite system (slab) that allows us to distinguish surface resonances and surface states for different surface terminations and separate them from the bulk states. Note that most of the surface electron states were observed for the Si-terminated surface of $GdRu_2Si_2$, where the topmost Gd layer is hidden by the Si–Ru–Si surface trilayer block. In our study, this surface will be the main focus.

First, our analysis of $GdRu_2Si_2$ will be focused on the characterization of the electronic structure in the paramagnetic phase, which shows a good agreement between experiment and theory. In the AFM ordered phase, our ARPES measurements reveal a pseudogap which is seen as a kind of a "sickle-moon" feature near the Fermi level (E_F) in the structure of the bulk projected bands taken along the $\bar{M}$–$\bar{X}$–$\bar{M}$ direction of the surface Brillouin zone (BZ). Our theoretical analysis indicates that this feature is directly linked with the formation of a spiral structure of Gd 4f moments within the basal plane. Furthermore, the agreement between the ARPES-derived electronic structure and the one based on DFT calculations enables a comprehensive characterization of bulk and surface states, including their properties and orbital compositions. Here, we found that in contrast to earlier predictions the FS near the Γ-point does not exhibit nesting properties. Instead, nesting occurs near the corner of the BZ with a vector along [100]([010]), which connects k_z-dispersion-less states with essential Gd d contribution. The size of the nesting vector fits well to describe the properties of the spiral magnetic structure. This indicates that the electronic states in this BZ region are most essential for a RKKY-mediated coupling of Gd 4f moments *via* Gd d states at the Fermi level. These results are in line with those recently reported in ref. 14. Lastly, we discuss the results of a theoretical modelling with stretching of the unit cell within the basal plane, analysing the modifications of the corner-nested region of the BZ. The obtained results allow us to propose the most plausible scenario for the emergence of the helical AFM phase in $GdRu_2Si_2$.

2 Results

2.1 Calculated electronic structure of the paramagnetic $GdRu_2Si_2$ (001) surfaces

We begin with a theoretical analysis of the surface electronic structure of the paramagnetic $GdRu_2Si_2$ obtained from *ab initio* DFT calculations. Similar to many other RET_2Si_2 materials,[15] the predominant cleavage plane of a single crystal of $GdRu_2Si_2$ (001) is between Si- and Gd-atomic layers,[11] leaving behind either a Si- or Gd-terminated surface. Therefore, to determine surface electron states and separate them from bulk electron bands, an asymmetric slab terminated by Si and Gd on either side was used allowing us to trace bulk-like bands, band gaps as well as surface-related states for both terminations. Thus, in this way, theoretically derived electron states for the Gd and Si surfaces of $GdRu_2Si_2$ (001) are shown in Fig. 1a and b, respectively. The surface electron states are shown in blue overlaid with the tan-colored k_z-projected bulk states. The latter are obtained by projecting the bulk electron bands of the paramagnetic spectrum (see ESI, Section A†) onto the (001) surface, perpendicular to the z direction. The strongly localized Gd 4f orbitals were treated as a frozen core approximation.

Both surfaces reveal a number of surface-related electron states. While some of them overlap strongly with the bulk bands, others reside within large projected band gaps. As we will see further, the theoretically derived spectral patterns agree well with those obtained in the momentum-resolved photoemission experiment. The in-gap surface states seen for the Si surface are almost fully localized within the topmost trilayer Si–Ru–Si block and are mainly composed of Ru 4d orbitals with different symmetries (lower panel of Fig. 1c). We mark a few examples of such states by using the colored (red, light blue and purple) circles in Fig. 1b and present their density profiles $|\Psi^2|$ in the upper panel of Fig. 1c. The lack of their overlap with the Gd layer makes these surface states rather insensitive to the stabilization of a spin-spiral magnetic order in the AFM phase of $GdRu_2Si_2$. However, other surface states considerably overlap with the bulk projected states and penetrate into their continuum. Hence, it is reasonable to anticipate that those states, like the one labelled in green situated between $\bar{\Gamma}$ and $\bar{X}$ close to the E_F, should get modified when the exotic magnetic order on the Gd sublattice sets in. We will discuss the sensitivity of these states to the magnetic order in detail later in comparison with our experimental ARPES results.

2.2 ARPES

To comprehensively explore the complex electronic structure of paramagnetic $GdRu_2Si_2$, we performed detailed ARPES measurements and compared the obtained results with those derived from our first principles calculations. In the first two rows of Fig. 2, we present the experimentally derived electronic structure taken from the Si-termination of a freshly cleaved $GdRu_2Si_2$ single crystal at 50 K along the $\bar{\Gamma}$–$\bar{M}$, $\bar{\Gamma}$–$\bar{X}$ and $\bar{X}$–$\bar{M}$ directions of the surface BZ. The ARPES pattern was obtained at a photon energy of 50 eV with horizontal (LH) and vertical (LV) polarizations shown in the first and second row of Fig. 2, respectively. In the third row, we display the k_z-projected bulk states along the same high-symmetry directions as in the experiment. Similar to Fig. 1, the tan-colored bulk states are overlaid with the slab-derived surface and surface-resonant states depicted in blue for the paramagnetic, Si-terminated $GdRu_2Si_2$ (001) surface.

The good agreement between experiment and theory allows us to easily identify and differentiate between the surface-

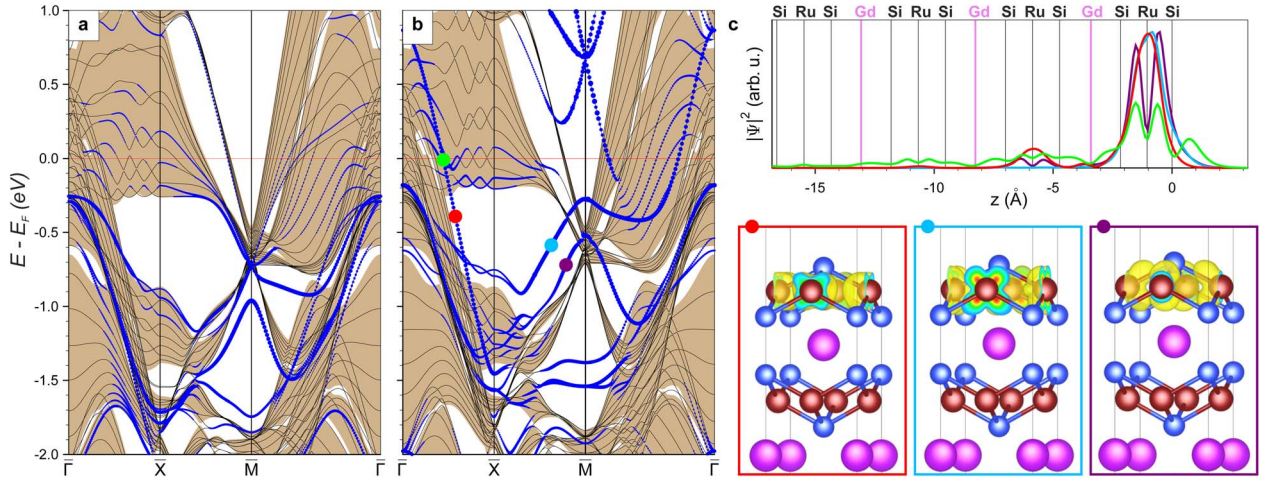

Fig. 1 Electronic structure of the paramagnetic phase of $GdRu_2Si_2$ (001) calculated for Gd- (a) and Si-terminated (b) surfaces. The tan-shaded area corresponds to the surface-projected bulk band structure, whereas the black lines are the result of a slab model. The size of blue dots reflects the weights of the surface states. Large colored circles in (b) mark the states whose spatial distribution is shown in (c) in the same colors. (c) Upper panel: electron density distribution (integrated over the *ab* plane) of the surface electron states marked in (b). Vertical lines reveal the positions of Gd (pink) and Si–Ru–Si (black) atomic layers. Lower panel: spatial distributions for the "red", "light blue", and "purple" surface states.

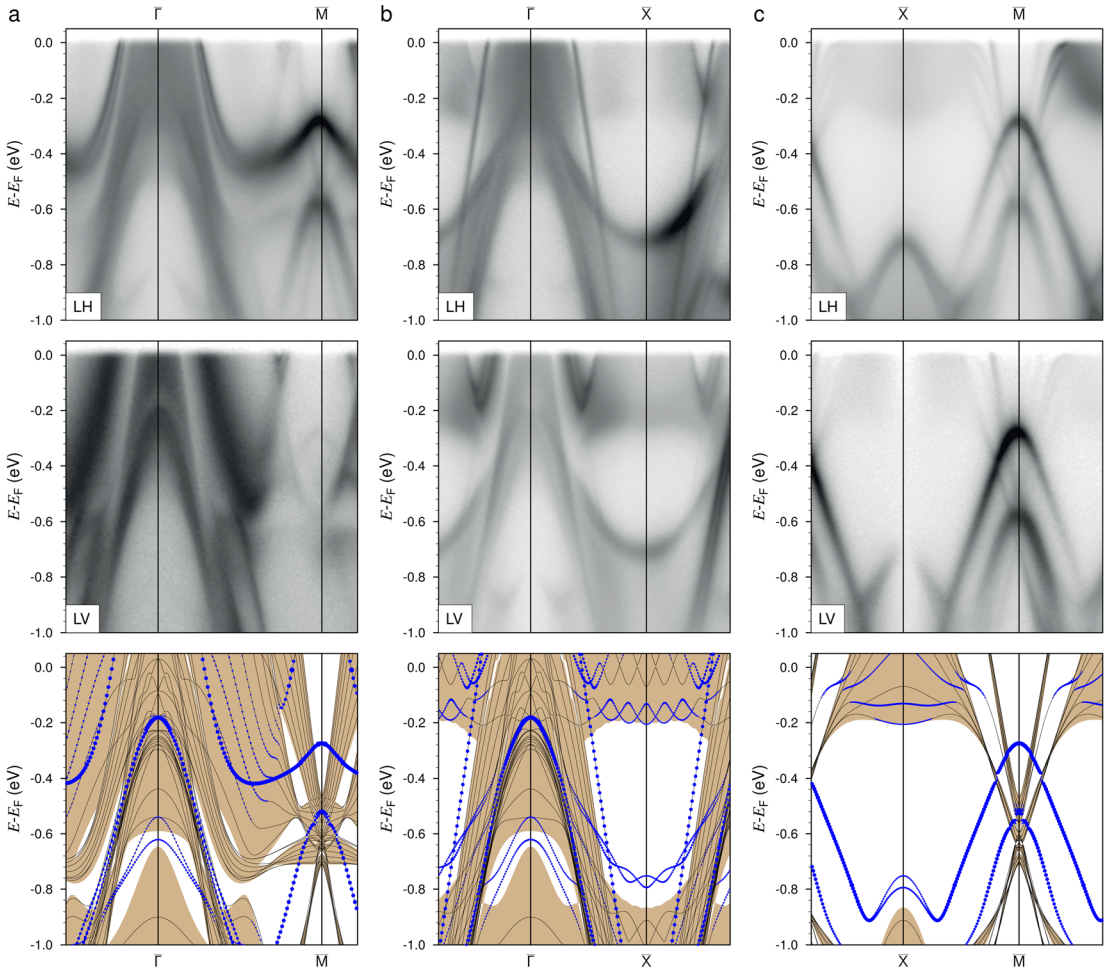

Fig. 2 Comparison between ARPES spectra and DFT-derived band structures for the paramagnetic Si-terminated (001) surface of $GdRu_2Si_2$ along $\bar{\Gamma}$–$\bar{M}$ (a), $\bar{\Gamma}$–$\bar{X}$ (b), and $\bar{X}$–$\bar{M}$ (c) directions measured with linear horizontal (LH) (top row) and linear vertical (LV) (middle row) light polarizations. The bottom row presents the DFT-derived band structure shown in the same energy window for better comparison with ARPES data.

related bands and the bulk-projected electronic structure in the ARPES patterns. This gives us a good starting point for the subsequent evaluation of how these states evolve when the peculiar spiral magnetic order of Gd 4f moments stabilizes in the AFM phase of $GdRu_2Si_2$. First, we will focus on the bulk states close to E_F, their properties and orbital composition. Based on ref. 10, special attention will be paid to the areas near high-symmetry points and, in particular, the center of the BZ. Secondly, we will investigate the behavior of the surface-related states which overlap with the bulk states (labelled in green in Fig. 1b). Lastly, we can then discuss and analyse the whole Fermi surface as derived from ARPES measurements and DFT calculations.

2.3 Effect of the spin spiral on the electronic structure of $GdRu_2Si_2$

After cooling the $GdRu_2Si_2$ sample below the spiral-AFM phase transition to a temperature of 19 K, we found that the ARPES patterns did not reveal large modifications of the electronic structure. Nevertheless, a number of subtle changes could be observed. One of the most visible changes is the emergence of a narrow bright feature ("pseudogap") in the bulk-projected spectrum, which can be seen as a kind of "sickle-moon" feature near E_F. This feature is presented in Fig. 3a in the ARPES data taken along the $\bar{M}$–$\bar{X}$–$\bar{M}$ direction of the surface BZ with the "pseudogap" being indicated by a blue arrow. For comparison, in Fig. 3b we show the projection of the calculated bulk states for the paramagnetic phase onto the same $\bar{M}$–$\bar{X}$–$\bar{M}$ direction of the surface BZ. This clearly demonstrates a homogeneous density of bulk states near the $\bar{X}$ point in the discussed vicinity of the Fermi level. Having observed the ARPES-derived signature of the spiral-AFM order of the Gd 4f moments, our next aim was a corresponding appropriate theoretical modeling. Being able to compute and achieve good agreement with the experiment would allow us to understand the ground state on the basis of first principles calculations the reasons for such a peculiar magnetic order in the AFM phase of $GdRu_2Si_2$.

To simulate the spiral-AFM phase, we constructed a bulk $5 \times 1 \times 1$ supercell, in which the spin spiral corresponding to $Q = 0.20$ (in units $2\pi/a$) is defined as schematically shown in Fig. 3c. In this supercell the spin magnetic moment on each subsequent Gd plane along the x direction is rotated by $\phi = 40°$. Note that it is slightly different from $\phi = 36°$ which corresponds to

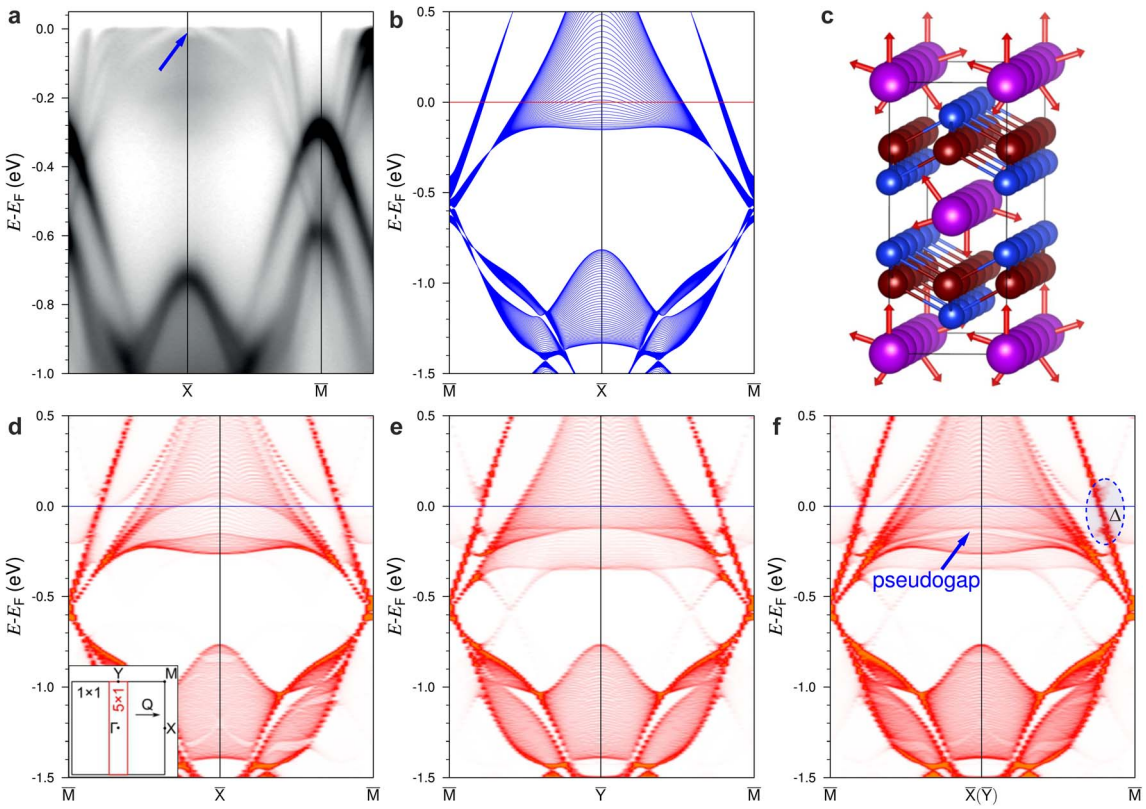

Fig. 3 (a) Low-temperature ARPES data taken at 19 K along the $\bar{M}$–$\bar{X}$–$\bar{M}$ direction of the surface BZ in the AFM phase of $GdRu_2Si_2$. A blue arrow indicates the "sickle-moon" shaped pseudogap which appears in the bulk continuum states below T_N. (b) Bulk electron states for paramagnetic $GdRu_2Si_2$ computed along the $\bar{M}$–$\bar{X}$–$\bar{M}$ direction and projected along k_z. (c) The $5 \times 1 \times 1$ supercell of $GdRu_2Si_2$ in the ordered phase where the Gd 4f moments are rotated within the yz-plane with a propagation vector of $Q = 0.2$ (in units $2\pi/a$), along the x direction. (d) The bulk-projected electron structure of the spiral-AFM ordered $GdRu_2Si_2$ calculated within the 5×1 supercell with the spin spiral propagated along x unfolded onto the $\bar{M}$–$\bar{X}$–$\bar{M}$ direction of the original 1×1 BZ. The inset shows the 1×1 (black) and 5×1 (red) BZs projected on (001). (e) The same as in panel (d) but for the $\bar{M}$–$\bar{Y}$–$\bar{M}$ direction. (f) Superposition of the bulk projected electron states shown in panels (d) and (e). The meaning of the highlighted Δ will be discussed later (see Fig. 6d and e).

the experimentally derived incommensurate spiral propagation vector of $Q = 0.22(2\pi/a)$.[4] As we will see below, the small difference of $Q = 0.20$ from $Q = 0.22$ is not essential for the following analysis. The k_z-projected bulk band structure unfolded onto the $\bar{M}$–$\bar{X}$–$\bar{M}$ direction (perpendicular to the spin spiral propagation, Fig. 3d) of the original 1 × 1 BZ shows that the main changes compared to the paramagnetic case occur close to the $\bar{X}$ point and near E_F where density of bulk states becomes inhomogeneous, having an increased density at the very bottom and a reduced one at E_F. The spectrum calculated along the $\bar{M}$–$\bar{Y}$–$\bar{M}$ direction (along the spin spiral propagation, Fig. 3e) also demonstrates its main changes at $\bar{Y}$ (which is equivalent to $\bar{X}$ in the original 1 × 1 BZ in the paramagnetic case); however, the reduced density can be found here at lower energies while the increased density lies at higher energies closer to E_F. Taking into account that the magnetic spirals along x and y directions must be equiprobable due to symmetry reasons, and that ARPES should acquire a mixture of magnetic domains with different spiral directions, the superposition of the spectra calculated for directions along and perpendicular to the magnetic spiral is presented in Fig. 3f, which shows the presence of a pseudogap in the continuum of the bulk states below E_F (a narrow area of a reduced density of the bulk states). This is in excellent agreement with the experiment. Thus, this observation serves as direct photoemission evidence for the presence of the spiral-AFM phase in the low-temperature limit.

2.4 Electronic structure of the Si-terminated surface of spiral-AFM $GdRu_2Si_2$

Next we explore how the spin-spiral AFM order is reflected in the properties of the surface electron states, in particular for the Si-terminated surface of $GdRu_2Si_2$. Fig. 4a and b show the ARPES data taken along the $\bar{\Gamma}$–$\bar{X}$ direction in the paramagnetic and spiral-AFM phase, respectively.

The spectra reveal prominent bands located in the energy range of −0.2 eV up to and crossing E_F. Our calculations allow us to identify these bands as surface resonances, which penetrate deep into the material overlapping with the bulk band states (Fig. 1b and c, marked in green). Below the spiral-AFM transition these states exhibit notable changes. Particularly, in the paramagnetic phase the photoemission intensity of these states varies smoothly along the spectral structure, while at low temperature an oscillatory modification of the intensity distribution can be observed. To reveal the origin of this intensity redistribution, we expand the 5 × 1 supercell bulk calculation to a supercell slab calculation for the spiral-AFM phase. Fig. 4c shows the spectrum of the Si-terminated (001) surface of $GdRu_2Si_2$ unfolded onto the $\bar{\Gamma}$–$\bar{X}$ (along the propagation of the spin spiral) and the $\bar{\Gamma}$–$\bar{Y}$ (perpendicular to the spin spiral) directions of the 1 × 1 BZ. Compared to the band structure of the paramagnetic phase (blue lines in Fig. 4c), both electronic structures almost coincide for the direction of the spiral propagation ($\bar{\Gamma}$–$\bar{X}$), whereas in the perpendicular direction ($\bar{\Gamma}$–$\bar{Y}$) the band distribution considerably changes.

Near E_F, the Gd 5d contribution to these states is almost equally determined by $d_{x^2-y^2}$ and $d_{xz}(d_{yz})$ orbitals (see Fig. 4d). With the spin spiral propagating along the x direction, the spin rotates in the yz-plane and clearly affects the d_{yz} orbitals but seems to have no influence on the d_{xz} orbital. Hence, when the surface resonant state penetrates into these bulk states, where the weight of Gd 5d orbitals is considerable, it should experience the effect of spiral-AFM order in the bulk. Again, due to the mixture of x- and y-spiral magnetic domains, in ARPES this modification manifests itself in both $-\bar{X}$–$\bar{\Gamma}$ and $\bar{\Gamma}$–$\bar{X}$ directions leading to a subtle but clearly notable effect.

2.5 Fermi surface and possible origin of the spin spiral

In ref. 10, the properties of the three-dimensional FS were intensively discussed. There, it was argued that nesting properties found in the center of the BZ are the key points for the formation of the spin-spiral magnetic order in the AFM phase of $GdRu_2Si_2$ and define the skyrmion physics in this material. To explore this point in detail, we present the calculated FS for the paramagnetic phase of $GdRu_2Si_2$ (Fig. 5a and b) with the experimentally derived FS from ARPES measurements (part of Fig. 5c). To simplify the analysis, we combine the ARPES data with the calculated band structure projected along the k_z direction onto the (001) surface as shown in the left side of

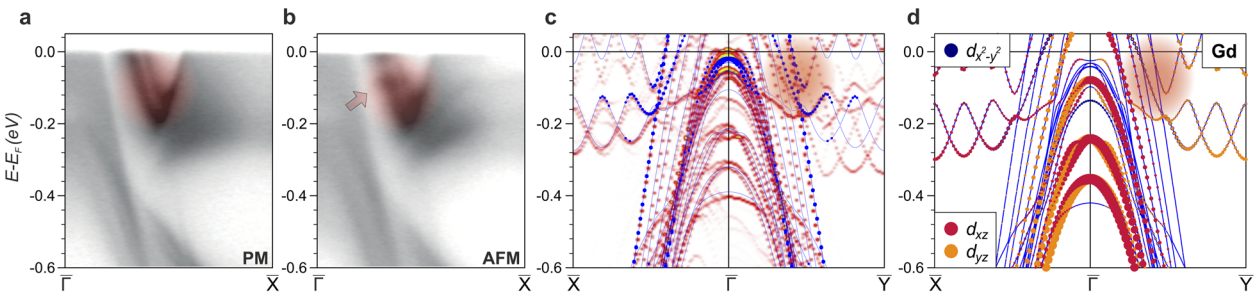

Fig. 4 ARPES data taken along the $\bar{\Gamma}$–$\bar{X}$ direction at 50 K (a) and at 19 K (b), that is, above and below the bulk T_N, respectively. The measurements were performed using a photon energy of 50 eV with linear vertical (s) polarization. The orange highlighted spot marks an area of the surface resonant state. (c) Unfolded calculated spectrum (shown in red) of the Si-terminated $GdRu_2Si_2$ (001) surface for the spiral-AFM phase along $\bar{\Gamma}$–$\bar{X}$ (along the propagation of the spin spiral) and $\bar{\Gamma}$–$\bar{Y}$ (perpendicular to the spin spiral) directions. The spectrum of the $GdRu_2Si_2$ slab of the same thickness for the paramagnetic phase is imposed (blue curves), and weights of the surface states are demonstrated by blue dots. (d) Weights of the Gd 5d orbitals for the paramagnetic phase.

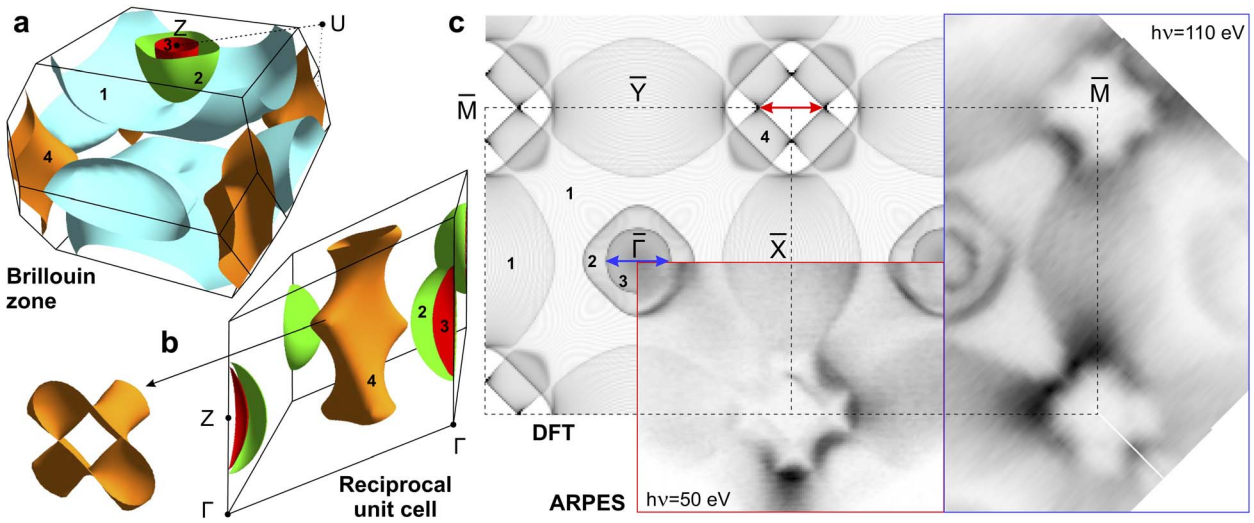

Fig. 5 Fermi surface (FS) for $GdRu_2Si_2$ in the paramagnetic phase presented for the first BZ (a) and for the reciprocal lattice unit (b). In panel (b), band 1 is not shown for simplicity; the left outset shows the top perspective view of band 4. (c) Projection of the calculated FS on the (001) surface. The red and blue framed parts show the ARPES-derived FS maps obtained with photon energies of $h\nu = 50$ eV and $h\nu = 110$ eV, respectively. The red arrow indicates the proposed nested region in the 3D FS while the blue arrow shows the region near the center of the BZ, which was discussed in ref. 10.

Fig. 5c. Based on this comparison, we see a close to perfect agreement between experiment and theory, indicating that our calculations reliably describe all bands in the vicinity of E_F. The four bands which form the FS are labeled as 1–4.

In ref. 10 it was proposed that band 3, which is highlighted in red in Fig. 5a and b, is mostly barrel-shaped and therefore provides good nesting conditions where the diameter of the barrel fits well to the wave number $Q = 0.22(2\pi/a)$ of the spin spiral. We indicate the respective region by using a blue arrow around the $\bar{\Gamma}$ point in Fig. 5c. However, based on our DFT results, we offer a different interpretation. First, we find that band 3 differs considerably more from a barrel-like shape than previously proposed and instead looks more ellipsoidal with a significant k_z dispersion centered around the Z-point of the BZ. In this regard, our calculations suggest that there are no strong nesting properties for this band.

On the other hand, our calculations indicate that band 4, which is situated around the $\bar{M}$ point, reveals nesting properties. This band shows almost no k_z-dispersion in the $\bar{M}$–$\bar{X}$ lateral direction. To better visualize this fact, we present in the outset of Fig. 5b the discussed band 4 from the top perspective. In this top view projection, it is clearly visible that the $\bar{M}$–$\bar{X}$ cuts have no k_z dispersion since they meet in single points. This nesting vector is highlighted by a red arrow at the corner of BZ in the FS shown in Fig. 5c. Furthermore, it is important to note that these points have a high density of states and possess a strong contribution from Gd 5d states, which are essential for the exchange interaction and will be discussed next.

To understand the relation between the spiral period and the features of the band structure, we analyze the orbital composition of the bands 1–4 at E_F. As illustrated in Fig. 6a, bands 1 and especially 4 have strong contributions from Gd 5d states, while bands 2 and 3 are mainly composed of Ru states with only a small contribution from Gd states (see detailed analysis of the orbital composition in ESI, Section A†). This allows us to conclude that band 4 not only fulfills the nesting condition, but also has the most significant admixture from Gd 5d-states, and thus is the most likely origin for the peculiar magnetic structure of $GdRu_2Si_2$.

Next, we will test the relation between the nesting vector and the spiral period. For this, we performed a series of *ab initio* calculations where the crystal lattice was stretched or compressed within the *ab* plane. Such deformations may lead to significant changes in the band structure as well as the spiral period, providing a possibility to explore the relationship between them. Fig. 6b demonstrates how the total energy evolves as a function of the spiral wave number Q for different values of stretching. Note that the shown curves are arbitrarily shifted in the energy scale for better comparison. For the case of the equilibrium lattice (black curve), the energy minimum is located at $Q = 0.20$, which is very close to the experimental value of $Q = 0.22$. Upon expansion of the lattice the minimum shifts to lower Q values until the system becomes ferromagnetic which happens at 11% of stretching. Upon compression of the lattice the global energy minimum turns to a local minimum, which shifts towards higher Q values and almost disappears at 2.5% of compression.

We can now determine how the band structure evolves under lattice deformation. For this, we will look in detail at the two most interesting bands, namely band 4, which we propose to be responsible for the spiral-AFM order since it exhibits strong nesting properties, and band 3, which was proposed in ref. 10. What we observe as a result of stretching is that band 4 shifts up in energy, while band 3 gets shifted down to lower energies. In both cases the related nesting vector becomes shorter, which is illustrated in Fig. 6c where the lengths of the proposed nesting vectors are shown as a function of stretching. The nesting vectors were measured along the Z–U direction of the BZ shown in Fig. 5a. Our results indicate a qualitative correlation between the length of the nesting vectors and the wave number of the

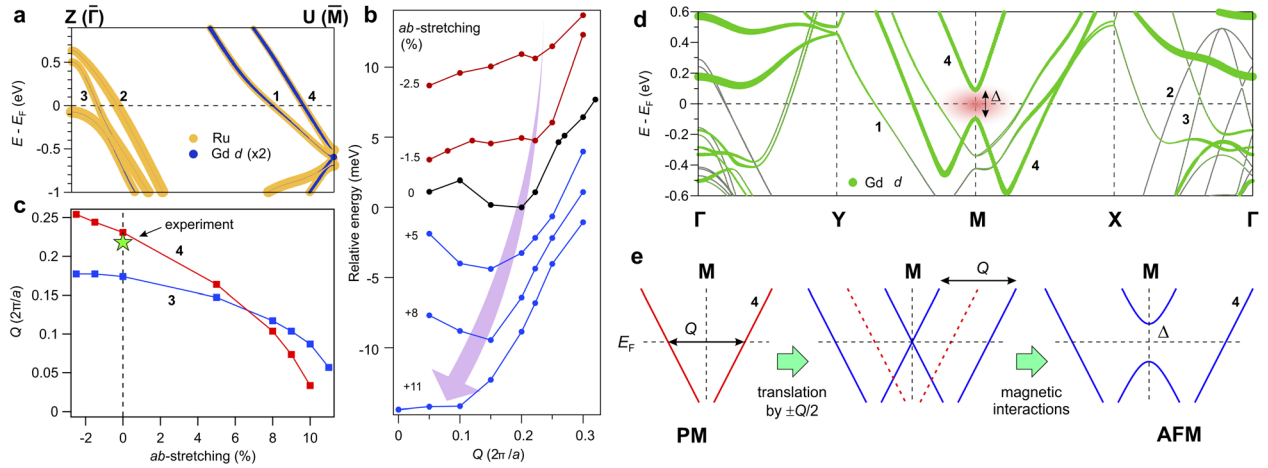

Fig. 6 (a) Electron band structure near the E_F calculated along the Z–U direction of the BZ (see Fig. 5a); the size of the colored symbols represents the weight of all states of Ru and 5d states of Gd, where the weight for the latter is multiplied by a factor of two. (b) The evolution of the total energy of the tetragonal cell as a function of the spin-spiral wave number Q. The cartoon arrow indicates how the minimum of total energy evolves upon lattice stretching. (c) Calculated evolution of the lengths of the red and blue $\vec{k}$ vectors shown in Fig. 5c for bands 3 and 4 at E_F. (d) Band structure of the spiral-AFM state with $Q = 0.22(2\pi/a)$, calculated using the tetragonal unit cell (the spiral vector $\vec{Q}$ is parallel to the Γ–X and Y–X directions). (e) Schematic illustration of the formation of band 4 in the direction along the spiral.

spiral. Upon stretching, the nesting vector gets shorter for both bands 3 and 4, while in the same way the spiral wave number becomes smaller. However, the experimental value of the wave number $Q = 0.22(2\pi/a)$ for the equilibrium lattice fits better to the nesting vector of band 4 than that of band 3 (experimental value shown as a green star in Fig. 6c). Additionally, the stretching value at which band 4 shifts above E_F coincides with the stretching value of 11% where the calculated Q becomes zero. Thus, in agreement with our previous statements about band 4, this band seems to be the probable candidate for the formation of the spin spiral *via* d–f hybridization.

To understand further the role of band 4 in the stabilization of the spiral state, we present the theoretical band structure of the spiral-AFM state in Fig. 6d. These calculations were performed using the so-called generalized Bloch conditions. In this formalism, for the case of a rotating spin, the wave function has the form of the following spinor

$$\Psi(\vec{r}) = \frac{1}{\sqrt{2}} \sum_{\vec{R}} \begin{pmatrix} e^{i(\vec{k}-\vec{Q}/2)\cdot\vec{R}} \phi^{\uparrow}(\vec{r}-\vec{R}) \\ e^{i(\vec{k}+\vec{Q}/2)\cdot\vec{R}} \phi^{\downarrow}(\vec{r}-\vec{R}) \end{pmatrix}, \quad (1)$$

summing over all unit cells. To ensure spin rotation, the quasi-momentum $\vec{k}$ gains an additional quantity of $\pm\vec{Q}/2$ that results in the respective translation of bands in the reciprocal space. This is schematically illustrated in Fig. 6e. In the paramagnetic phase, the states of band 4 at E_F at the two sides of the M point are separated by the nesting vector $\vec{Q}$ which coincides with the spin spiral wave vector. Upon translation by $\pm\vec{Q}/2$ the two sides of the band cross at the M point. The exchange interaction results in the opening of a magnetic gap Δ at the M point. The related decrease in the energy of the occupied states results in stabilization of the spiral. At the same time, bands 2 and 3 remain almost unchanged due to the small contribution of the Gd 5d orbitals.

It is worth noting that an experimental observation of the predicted magnetic gap with ARPES is very challenging. First, the band structure in Fig. 6d cannot be directly compared with ARPES data because of the redefinition of the quasimomentum $\vec{k}$. The experimental measurements have to be compared with the unfolded bands from the supercell calculations shown in Fig. 3f. One can see that the discussed gap Δ in band 4 is present in the supercell calculation, although it appears shifted by $\vec{Q}/2$ from the $\bar{M}$ point. Moreover, it does not look like a real gap since it is formed only between the low-intensity replica bands which cannot be reliably detected in our ARPES data. Instead, we were able to detect the aforementioned pseudogap formed in band 1 that is of magnetic origin and thus indicates the formation of the spiral-AFM state.

2.6 Magnetic interaction

To understand in more detail the nature of magnetic interaction in the system, we calculated exchange coupling constants from first-principles calculations applying the magnetic force theorem as it is implemented within the multiple scattering theory.[16,17] The exchange coupling constants, J_{ij} represent the direct and indirect overlap between wave functions participating in the magnetic interaction between atoms i and j. A full Fourier transform, $J(\vec{Q})$ is proportional to the total energy, whose minimum, *i.e.* the ground state, corresponds to the maximum of $J(\vec{Q})$. To determine the ground state, $J(\vec{Q})$ was computed along high symmetry directions of the BZ using various density functional approximations. The HSE06 hybrid functional is the best approach for describing the magnetic bulk band structure of $GdRu_2Si_2$ (see the discussion in ESI, Section A†). Unfortunately, this method is not yet implemented within the multiple scattering theory. Therefore, we used a GGA + U functional to obtain exchange coupling constants. It should be noted that previously reported first-principles studies of this

system were carried out using a bare GGA functional.[10,12] Unfortunately, the GGA + U approximation cannot fully reproduce the band structure obtained with the HSE06 hybrid functional. Nevertheless, the Gd 4f states are pushed down in energy within this approach and the band structure in the Fermi level vicinity with the exception of several features looks similar to that obtained within the HSE06 functional (ESI, Section A†).

$J(\vec{Q})$ calculated along the high symmetry directions show three peaks: one is between Γ and X, the second is between X and M, and the third is between Γ and Z (see ESI, Section B and Fig. S2a†). The global maximum, which corresponds to the total energy minimum, determines a spiral magnetic structure within the Gd layer. The Q vector of this maximum is in a good agreement with our calculations within generalized Bloch conditions and experiments. However the presence of two other peaks with similar magnitudes indicates a competition between three various magnetic orders: two intra- and one inter-layer spirals. We point out here that the results might be not fully correct, since the approximation used does not provide a full agreement with the HSE06 hybrid functional calculations. Another approach we have tried, a self-interaction correction (SIC) method, delivers a similar picture (see ESI, Fig. S2b†), although $J(\vec{Q})$ is about two times smaller than that obtained within the GGA + U approach. The latter fact is because the SIC method usually overestimates the localization of SI-corrected orbitals. However, both approaches predict a similar magnetic structure.

The next question arises about the origin of spirals in $GdRu_2Si_2$. A structurally similar system, $GdRh_2Si_2$, exhibits a robust layerwise antiferromagnetic ordering with a relatively high Néel temperature of 107 K.[18] We think there are two main reasons for such a strong difference between these two AFM materials. First, Rh has one 4d electron more than Ru. Therefore, Rh–Si hybridization is essentially distinct from that between Ru and Si atoms. The additional Rh 4d electron weakens the Gd–Si coupling and Gd has more 5d electrons for the intra-layer magnetic coupling between the Gd 4f local moments, which results in a strong ferromagnetic order within the Gd layers. Indeed, the magnetic interaction between the nearest Gd moments in $GdRh_2Si_2$ is much stronger than that in $GdRu_2Si_2$: 5.1 meV *vs.* 0.7 meV, while the inter-layer magnetic coupling in both systems is of a similar magnitude. The second reason for the stronger intra-layer coupling in $GdRh_2Si_2$ is the slight difference in the lattice parameters in these materials. Lanthanides are well known for a sensitive dependence of their magnetic properties on the structure. Thus, a strong reduction of the intra-layer magnetic interaction in $GdRu_2Si_2$ leads to magnetic frustration and spiral formation in this material. Our analysis indicates that the magnetic interaction between Gd 4f local moments is mainly mediated by conduction electrons. Although our ARPES experiments and DFT calculations do not confirm the nesting found in ref. 10, the magnitude of the respective vector which was discussed in ref. 10 is similar to that of the nesting vector at the corner of the BZ which was found in our study. Combining our finding and the discussion made in ref. 10 we conclude that the RKKY interaction is the dominant mechanism for helical magnetism in this system. The helical magnetic order arises due to a competition of in-plane and out-of-plane antiferromagnetic interactions, which could lead to a skyrmion formation without a strong spin–orbit coupling in the system.[19]

3 Conclusions

In summary, applying momentum-resolved photoemission measurements and *ab initio* DFT calculations, we explored the bulk and surface electronic structure of the helical antiferromagnetic material $GdRu_2Si_2$. The ARPES-derived data, taken for $GdRu_2Si_2$ in the paramagnetic phase, reveal sharp patterns containing the surface and bulk-projected electron states which allow the exploration of how these states are modified upon the PM–AFM phase transition. Comparison of the ARPES data taken from the AFM phase of $GdRu_2Si_2$ with the results of *ab initio* DFT calculations allowed us to identify the bulk-related states which are intrinsic for the spiral order of 4f moments. Namely, we detected a pseudogap within the bulk continuum states close to E_F which is seen as a "sickle-moon" shaped spectral feature. A rather good agreement of experimental and theoretical results allowed us to characterize in detail the properties and orbital composition of the Fermi surface of $GdRu_2Si_2$. Note that our results do not confirm the prediction of the existence of the nested three-dimensional barrel-shaped FS near the Γ-point which was reported recently.[10] Instead, we found a nested FS sheet at the corner of the BZ, supporting the recent results reported in ref. 14. Our theoretical analysis suggests that this feature possesses a strong admixture of 5d-states of Gd. We show that stretching or compressing the crystal lattice within the *ab* plane essentially influences the Gd 5d states nesting vector and consequently changes the period of the magnetic spiral in the Gd 4f spin channel. The obtained results allow us to conclude that the RKKY interaction is the most plausible mechanism which defines the spiral magnetic order in $GdRu_2Si_2$ and is responsible for the emergence of skyrmions in this material. Although in $GdRu_2Si_2$ the skyrmion phase emerged at rather low temperature the deep understanding of the underlying skyrmion physics in the centrosymmetric systems may help to predict novel materials where the nano-size skyrmions may appear at essentially higher temperature, and perhaps even at room temperature. Essentially, in this centrosymmetric type of compound with the $ThCr_2Si_2$ structure type, multiple magnetic systems with d- and f-magnetic moments exist, partially with rather high ordering temperatures (for a review see M. Shatruk[20]). In particular, in the discussed class of materials there are some antiferromagnets, like $CeCo_2P_2$ with a rather high temperature of the magnetic order ($T_N = 440$ K).[21,22] Since magnetism in most of the rare earth compounds with a centrosymmetric crystal structure is mainly driven by the RKKY interaction, these systems can be promising to develop magnetic skyrmions without a strong Dzyaloshinskii–Moriya interaction.

4 Methods

Single crystals of $GdRu_2Si_2$ were grown from indium flux using high purity starting materials Gd (99.9%, EvoChem), Ru (99.95%, EvoChem), Si (99.9999%, Wacker) and In (99.9995%, Schuckard) and a modified Bridgman method as described in ref. 23. Gd, Ru, Si, and In were used in the ratio of Gd : Ru : Si : In

= 1 : 2 : 2 : 24. The crystal growth was performed in a vertical furnace (GERO HTRV 70-250/18) (T_{max} = 1600 °C), with a slow cooling period with a rate of 1–4 K h^{-1} down to 850 °C followed by fast cooling to room temperature with 300 K h^{-1}. The crystals were separated from the flux by etching in hydrochloric acid. We obtained platelet-shaped crystals with typical dimensions of 3 mm × 3 mm and a thickness of 50–100 μm.

ARPES experiments were performed at the ULTRA endstation of the SIS-X09LA beamline, Swiss Light Source, and at the BLOCH beamline, MAX-IV laboratory in Lund. Both ARPES endstations were equipped with a Scienta R4000 analyser. The single-crystal samples of $GdRu_2Si_2$ were cleaved *in situ* under ultra-high vacuum conditions better than 10^{-10} mbar.

Electronic structure calculations were carried out within the density functional theory using the projector augmented-wave (PAW) method[24,25] as implemented in the VASP code.[26] The exchange–correlation energy was treated using the generalized gradient approximation[27] for most calculations. The Gd potential when strongly localized valence 4f electrons are treated as core states was used for non-magnetic calculations. The standard Gd potential in which the 4f electrons are treated as valence states was used for spin-polarized calculations of magnetic phases. To correctly describe the highly correlated Gd 4f electrons, we include the correlation effects within both the HSE06 screened hybrid functional[28] and the GGA + *U* method.[29] The values of *U* and *J* parameters were taken to be 6.7 eV and 0.7 eV, respectively, which give a good agreement with the HSE06 band structure. Additionally we use the Slater-type DFT-1/2 self-energy correction method[30,31] with a partially (quaternary) ionized silicon potential for better describing hybridization between deep Gd f and Si p_{xy} orbitals. To simulate the spiral magnetic state we consider spin spirals with two different methods. The first is to explicitly construct the spiral in a supercell using noncollinear magnetic moments in the *yz*-plane, perpendicular to the spin spiral propagation vector (along the *x* direction) and the second approach is to use a spin spiral method to simulate spirals in the unit cell with generalized Bloch conditions.[32] In the first case we use BandUP code[33,34] to unfold the supercell band structure onto the 1 × 1 BZ. Additional band structure calculations for the paramagnetic phase (Fig. 5c) were performed with the Gd 4f states in the core using FPLO-18.00-52 code (improved version of the original FPLO code by K. Koepernik and H. Eschrig[35]). The results are in perfect agreement with those obtained with the VASP code. All presented ball-and-stick atomic structures were visualized with VESTA.[36] The Fermi surface was determined on a dense 27 × 27 × 23 *k*-point mesh and visualized by using FermiSurfer.[37]

Author contributions

S. V. E. – conceptualization, formal analysis, methodology, project administration, writing – original draft, writing – review & editing; D. G. – investigation, data curation, formal analysis; G. P. – investigation, data curation, formal analysis; A. K. – investigation, data curation, formal analysis; K. A. – investigation, data curation, formal analysis; A. V. T. – investigation, data curation, formal analysis; S. S. – investigation, data curation, formal analysis; K. K. – investigation, resources, data curation, formal analysis; E. V. C. – investigation, funding acquisition; V. S. S. – investigation, funding acquisition; A. E. – investigation, software, writing – review & editing; C. K. – conceptualization, investigation, resources, project administration, writing – review & editing, funding acquisition; D. Y. U. – conceptualization, investigation, project administration, writing – original draft, writing – review & editing; D. V. V. – conceptualization, investigation, project administration, writing – original draft, writing – review & editing.

Conflicts of interest

There are no conflicts to declare.

Acknowledgements

We acknowledge the German Research Foundation (DFG) for the support through the grants no. KR3831/5-1, no. LA655/20-1, SFB1143 (project no. 247310070), and TRR288 (no. 422213477, project no. A03). The density functional theory calculations were supported by the Government research assignment for ISPMS SB RAS (project FWRW-2022-0001). E. V. C. acknowledges support from Saint Petersburg State University (project ID no. 94031444). V. S. S. and D. Y. U. work was partially supported by the Ministry of Science and Higher Education of the Russian Federation (no. FSMG-2023-0014) and RSF 23-72-30004. The calculations were partially performed using the equipment of the Shared Resource Center "Far Eastern Computing Resource" of IACP FEB RAS (**https://cc.dvo.ru**) and Joint Supercomputer Center of the Russian Academy of Sciences (**https://rscgroup.ru/en/project/jscc**). We also thank the Paul Scherrer Institut, Villigen, Switzerland, for the allocation of ARPES experiments at the ULTRA endstation of the SIS-X09LA beamline of the Swiss Light Source. We acknowledge MAX IV Laboratory for experimental time on beamline BLOCH under proposal 20211066. Research conducted at MAX IV, a Swedish national user facility, was supported by the Swedish Research Council under contract 2018-07152, the Swedish Governmental Agency for Innovation Systems under contract 2018-04969, and Formas under contract 2019-0249.

References

1 M. Ślaski and A. Szytuła, *J. Less-Common Met.*, 1982, **87**, L1–L3.
2 K. Hiebl, C. Horvath, P. Rogl and M. J. Sienko, *J. Magn. Magn. Mater.*, 1983, **37**, 287–296.
3 M. Ślaski, A. Szytuła, J. Leciejewicz and A. Zygmunt, *J. Magn. Magn. Mater.*, 1984, **46**, 114–122.
4 N. D. Khanh, T. Nakajima, X. Yu, S. Gao, K. Shibata, M. Hirschberger, Y. Yamasaki, H. Sagayama, H. Nakao, L. Peng, K. Nakajima, T. Takagi, R. Arima, Y. Tokura and S. Seki, *Nat. Nanotechnol.*, 2020, **15**, 444–449.
5 A. Garnier, D. Gignoux, N. Iwata, D. Schmitt, T. Shigeoka and F. Zhang, *J. Magn. Magn. Mater.*, 1995, **140–144**, 899–900.

6 M. Rotter, M. Doerr, M. Zschintzsch, A. Lindbaum, H. Sassik and G. Behr, *J. Magn. Magn. Mater.*, 2007, **310**, 1383–1385.
7 T. Samanta, I. Das and S. Banerjee, *J. Appl. Phys.*, 2008, **104**, 123901.
8 A. Garnier, D. Gignoux, D. Schmitt and T. Shigeoka, *Phys. B*, 1996, **222**, 80–86.
9 J. Prokleška, J. Vejpravová and V. Sechovský, *J. Phys.: Conf. Ser.*, 2006, **51**, 127.
10 J. Bouaziz, E. Mendive-Tapia, S. Blügel and J. B. Staunton, *Phys. Rev. Lett.*, 2022, **128**, 157206.
11 Y. Yasui, C. J. Butler, N. D. Khanh, S. Hayami, T. Nomoto, T. Hanaguri, Y. Motome, R. Arita, T. Arima, Y. Tokura and S. Seki, *Nat. Commun.*, 2020, **11**, 5925.
12 T. Nomoto, T. Koretsune and R. Arita, *Phys. Rev. Lett.*, 2020, **125**, 117204.
13 S. Hayami and Y. Motome, *Phys. Rev. B*, 2021, **103**, 024439.
14 N. Matsuyama, T. Nomura, S. Imajo, T. Nomoto, R. Arita, K. Sudo, M. Kimata, N. D. Khanh, R. Takagi, Y. Tokura, S. Seki, K. Kindo and Y. Kohama, *Phys. Rev. B*, 2023, **107**, 104421.
15 G. Bihlmayer, P. Noel, D. V. Vyalikh, E. V. Chulkov and A. Manchon, *Nat. Rev. Phys.*, 2022, **4**, 642.
16 A. Liechtenstein, M. Katsnelson, V. Antropov and V. Gubanov, *J. Magn. Magn. Mater.*, 1987, **67**, 65–74.
17 M. Hoffmann, A. Ernst, W. Hergert, V. N. Antonov, W. A. Adeagbo, R. M. Geilhufe and H. B. Hamed, *Phys. Status Solidi B*, 2020, **257**, 1900671.
18 M. Güttler, A. Generalov, M. M. Otrokov, K. Kummer, K. Kliemt, A. Fedorov, A. Chikina, S. Danzenbächer, S. Schulz, E. V. Chulkov, Y. M. Koroteev, N. Caroca-Canales, M. Shi, M. Radovic, C. Geibel, C. Laubschat, P. Dudin, T. K. Kim, M. Hoesch, C. Krellner and D. V. Vyalikh, *Sci. Rep.*, 2016, **6**, 24254.
19 T. Okubo, S. Chung and H. Kawamura, *Phys. Rev. Lett.*, 2012, **108**, 017206.
20 M. Shatruk, *J. Solid State Chem.*, 2019, **272**, 198–209.
21 G. Poelchen, I. P. Rusinov, S. Schulz, M. Güttler, M. Mende, A. Generalov, D. Y. Usachov, S. Danzenbächer, J. Hellwig, M. Peters, K. Kliemt, Y. Kucherenko, V. N. Antonov, C. Laubschat, E. V. Chulkov, A. Ernst, K. Kummer, C. Krellner and D. V. Vyalikh, *ACS Nano*, 2022, **16**, 3573–3581.
22 G. Poelchen, J. Hellwig, M. Peters, D. Y. Usachov, K. Kliemt, C. Laubschat, P. M. Echenique, E. V. Chulkov, C. Krellner, S. S. P. Parkin, D. V. Vyalikh, A. Ernst and K. Kummer, *Nat. Commun.*, 2023, **14**, 5422.
23 K. Kliemt, M. Peters, F. Feldmann, A. Kraiker, D.-M. Tran, S. Rongstock, J. Hellwig, S. Witt, M. Bolte and C. Krellner, *Cryst. Res. Technol.*, 2020, **55**, 1900116.
24 P. E. Blöchl, *Phys. Rev. B: Condens. Matter Mater. Phys.*, 1994, **50**, 17953–17979.
25 G. Kresse and D. Joubert, *Phys. Rev. B: Condens. Matter Mater. Phys.*, 1999, **59**, 1758–1775.
26 G. Kresse and J. Furthmüller, *Phys. Rev. B: Condens. Matter Mater. Phys.*, 1996, **54**, 11169–11186.
27 J. P. Perdew, K. Burke and M. Ernzerhof, *Phys. Rev. Lett.*, 1996, **77**, 3865–3868.
28 A. V. Krukau, O. A. Vydrov, A. F. Izmaylov and G. E. Scuseria, *J. Chem. Phys.*, 2006, **125**, 224106.
29 V. I. Anisimov, J. Zaanen and O. K. Andersen, *Phys. Rev. B: Condens. Matter Mater. Phys.*, 1991, **44**, 943–954.
30 L. G. Ferreira, M. Marques and L. K. Teles, *Phys. Rev. B: Condens. Matter Mater. Phys.*, 2008, **78**, 125116.
31 L. G. Ferreira, M. Marques and L. K. Teles, *AIP Adv.*, 2011, **1**, 032119.
32 L. M. Sandratskii, *Adv. Phys.*, 1998, **47**, 91–160.
33 P. V. C. Medeiros, S. Stafström and J. Björk, *Phys. Rev. B: Condens. Matter Mater. Phys.*, 2014, **89**, 041407.
34 P. V. C. Medeiros, S. S. Tsirkin, S. Stafström and J. Björk, *Phys. Rev. B: Condens. Matter Mater. Phys.*, 2015, **91**, 041116.
35 K. Koepernik and H. Eschrig, *Phys. Rev. B: Condens. Matter Mater. Phys.*, 1999, **59**, 1743–1757.
36 K. Momma and F. Izumi, *J. Appl. Crystallogr.*, 2011, **44**, 1272–1276.
37 M. Kawamura, *Comput. Phys. Commun.*, 2019, **239**, 197–203.